Industrial Crops & Products 204 (2023) 117184

Contents lists available at ScienceDirect

Industrial Crops & Products

journal homepage: www.elsevier.com/locate/indcrop

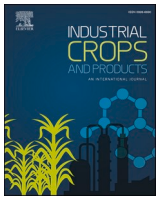

Biochar activated by potassium carbonate to load organic phase change material: Better performance and environmental friendliness

Laiquan Lv [a], Shengyao Huang [a], Chengyue Zhou [b], Weiwei Ma [a,c,*]

[a] key Laboratory of Clean Energy and Carbon Neutrality of Zhejiang Province, Jiaxing Research Institute, Zhejiang University, Jiaxing 314031, PR China
[b] Zhejiang Hangzhou High School, Hangzhou 310003, PR China
[c] State Key Laboratory of Clean Energy Utilization, Institute for Thermal Power Engineering, Zhejiang University, Hangzhou 310027, PR China

ARTICLE INFO

Keywords:
Activated biochar
Organic phase change materials
Shape-stable
Thermal conductivity
Latent heat energy storage

ABSTRACT

Chemically activated biochar, which is characterized by its high surface area, thermal stability, and chemical compatibility, exhibits great potential for loading phase change material (PCM) to enhance heat transfer and prevent leakage. However, conventional chemical activation processes typically involve highly corrosive and toxic chemical activators that pose environmental hazards. Biochar that is activated by K_2CO_3, which achieves high porosity while minimizing adverse environmental effects, has been applied in some fields. In this study, K_2CO_3 was employed as a chemical activator, and five waste biomass materials were utilized as precursors to produce biochar samples for the loading of paraffin (PA), stearic acid (SA), and polyethylene glycol (PEG). The results revealed that the activated biochar derived from corncob (CC) exhibited remarkable textural characteristics, and it had a specific surface area of 1053.95 m^2/g and a total pore volume of 0.467 cm^3/g. Additionally, owing to its larger specific surface area and richer textural characteristics, the loading capacities of CC for PA, SA, and PEG were as high as 78.79 %, 80.83 %, and 85.19 %, respectively. Furthermore, introducing PA, SA, and PEG into CC resulted in thermal conductivity enhancements of 1.460-, 1.138-, and 1.271-fold, respectively. Lastly, incorporating biochar improved the thermal stability of the composite PCMs. This study aimed to explore the performance of the biochar activated by K_2CO_3 in PCM loading, enhancing the environmental sustainability of waste biomass-derived activated biochar in PCM loading applications.

1. Introduction

Humanity's heavy reliance on fossil fuels, along with the inherent limitations and unsustainable consumption of these fuels, has resulted in a genuine crisis that is hindering sustainable human development (Grasso and Heede, 2023; Londoño-Pulgarin et al., 2021). The global energy landscape and supply-demand dynamics are undergoing significant adjustment and transformation, which has brought about a need to establish a reliable and efficient energy system centered around clean energy (Ahmed et al., 2022). This transition represents a global consensus and an irreversible trend toward a new era of energy (Wei et al., 2018a). The robust development of clean energy, and renewable energy in particular, plays a crucial role in addressing and overcoming the inherent drawbacks of fossil fuels. Nonetheless, the availability of renewable energy is limited and involves spatial constraints. Thermal energy storage (TES) has emerged as an effective solution with which to tackle these challenges (López-Sabirón et al., 2014).

As one form of TES, latent heat storage has garnered considerable interest because of its notable energy storage density and isothermal behavior during phase transition (Nazir et al., 2019). Phase change materials (PCMs) absorb or release latent heat during melting or solidification, which allows for efficient energy storage and retrieval. However, there are two challenges in utilizing PCMs for TES applications, which are the low thermal conductivity and susceptibility to leakage of PCMs, which limits the heat transfer rate and introduces a threat to safety (Han et al., 2022). The leakage of PCM poses a risk of system failure and can potentially impact the safety of equipment and individuals. To address this concern, researchers have proposed various methods to prevent PCM leakages, such as microencapsulated PCM (Choi et al., 2022), shape-stable PCM (Xu et al., 2023), and macro-packed PCM (Yun et al., 2022).

Furthermore, carbon support materials have emerged as a promising solution (Singh et al., 2022). Carbon-based materials, such as expanded

* Corresponding author at: key Laboratory of Clean Energy and Carbon Neutrality of Zhejiang Province, Jiaxing Research Institute, Zhejiang University, Jiaxing 314031, PR China.
E-mail address: mww502@zju.edu.cn (W. Ma).

https://doi.org/10.1016/j.indcrop.2023.117184
Received 3 June 2023; Received in revised form 15 July 2023; Accepted 18 July 2023
Available online 14 August 2023

Nomenclature

Abbreviation

AB	activated biochar.
BB	bamboo activated biochar.
BET	Brunauer-Emmett-Teller.
BJH	Barrett-Joyner-Halenda.
CC	corncob activated biochar.
CNT	carbon nanotube.
CPCM	composite phase change material.
DSC	differential scanning calorimetry.
DTG	derivative thermogravimetry.
EG	expanded graphite.
FT-IR	Fourier transform infrared.
PA	paraffin.
PEG	polyethylene glycol.
PCM	phase change material.
PN	pine wood activated biochar.
RH	rice husk activated biochar.
SA	stearic acid.
SEM	scanning electron microscope.
TES	thermal energy storage.
TG	thermogravimetry.
WS	walnut shell activated biochar.
XRD	X-ray diffraction.

symbols

C	loading capacity [%].
$D_{average}$	average pore diameter [nm].
E	loading efficiency [%].
m	mass [g].
R	empirical parameter.
S_{BET}	BET specific surface area [m^2/g].
T_m	peak melting temperature [°C].
T_s	peak solidification temperature [°C].
V_{total}	total pore volume [cm^3/g].
$W_{precursor}$	mass of biomass precursor [g].
W_{AB}	mass of biochar activated by K_2CO_3 [g].
Y	yield of biochar [%].
η	influence degree [%].
ΔH_{endo}	endothermic enthalpy [kJ/kg].
ΔH_{exo}	exothermic enthalpy [kJ/kg].

graphite (EG) (Zhou et al., 2021), carbon nanotubes (CNTs) (Cong et al., 2021), and graphene (Fan et al., 2014), possess excellent thermal conductivity, and can be employed as additives or matrices to enhance the thermal performance of PCMs. Incorporating carbon support materials into PCM composites can significantly improve their thermal conductivity (Yadav et al., 2021). Moreover, carbon support materials offer advantages such as light weight, high surface area, chemical stability, and tunable properties, which make them suitable candidates for TES applications. The capillary force and surface tension provided by the richly porous structure of these materials can effectively load PCMs, which ensures that liquid PCM does not leak and thereby improves the overall performance and reliability of TES systems (Stonehouse and Abeykoon, 2022).

Although these carbon support materials have demonstrated certain advantages in enhancing the performance of PCMs, they do have drawbacks and present some challenges. These materials face limitations in large-scale applications due to their high production costs (Atinafu et al., 2021b). Additionally, they often exhibit poor dispersion and stability, which leads to spontaneous aggregation behavior (Su et al., 2022; Yang et al., 2022). Moreover, their production may involve chemical treatment agents and high temperatures, which can introduce harmful substances and further increase production costs (Lv et al., 2022).

Biochar, which is a carbon-rich material derived from the pyrolysis of biomass, such as agricultural waste, wood, or organic residues, offers unique advantages as a carbon support material for TES applications (Li et al., 2023). Integrating biochar into TES systems enhances the energy storage of the system and promotes the utilization of biomass waste in a sustainable and environmentally friendly manner (Amalina et al., 2022a; Amalina et al., 2022b). Biochar production methods include pyrolysis (Das et al., 2020), hydrothermal carbonization (Shen, 2020; Sinan and Unur, 2017), torrefaction (Grycova et al., 2020; He et al., 2018), and gasification (Akhtar et al., 2018; Elliott, 2008), among others. Of these methods, pyrolysis has garnered considerable attention owing to its durability, high carbon content, favorable stability, and adaptability to diverse biomass feedstocks for biochar production (Venkatachalam et al., 2023). Das et al. (2020) employed an intermittent pyrolysis method at 550 °C to produce biochar from aquatic invasive weed plants for paraffin (PA) loading. The resulting biochar exhibited a specific surface area of 14.001 m^2/g, and the optimal mixing ratio of biochar to PCM was determined to be 6:4. Atinafu et al. (2021b) utilized commercial biochar produced via pyrolysis at 550 and 700 °C as a support material for loading n-eicosane. Their research findings revealed that the loading efficiencies of the two types of biochar for PCM were 26.4 % and 37.1 %, respectively, with corresponding latent heat values of 75 and 52 kJ/kg. Yang et al. (2018) conducted a carbonization of poplar wood at 500 °C for 2 h in a nitrogen atmosphere, followed by a sintering process at 1000 °C for 2 h to obtain carbonized wood for the loading of 1-tetradecanol. The resulting carbonized wood exhibited a specific surface area of 235.37 m^2/g and displayed a high PCM loading capacity, that reached 73.4 %. In a separate study, Gu et al. (2019) produced composite PCMs by blending PA with biochar derived from the carbonization of chili straw at 300 °C for 1 h, followed by further carbonization at 600 °C for 0.5 h. The prepared biochar demonstrated a specific surface area of 5.0611 m^2/g, and its loading capacity for PCM was 50 %.

Furthermore, various approaches, including physical, chemical, and biological activation methods, have been proposed to activate biochar so that it severs as a functional carbon. These approaches are intended to improve the specific surface area and porosity of biochar (Marsh and Rodríguez-Reinoso, 2006; Nicholas et al., 2019). In terms of physical activation methods, previous studies have reported on the specific surface areas of steam-activated biochar derived from bamboo (Wang et al., 2020), canola straw, manure pellet, sawdust, wheat straw (Kwak et al., 2019), and wood apple fruit shell (Chakraborty et al., 2018), which were 2.12, 106, 5.1, 356, 316, and 308 m^2/g, respectively. Lv et al. (2022) obtained biochar and physically activated biochar through the pyrolysis of waste phoenix leaf at different temperatures, followed by physical activation using CO_2 and steam. The specific surface areas of the biochar after pyrolysis at 500 °C and activation by CO_2 and steam were 14.182, 139.400, and 421.993 m^2/g, with corresponding loading capacities for polyethylene glycol (PEG) of 69.41 %, 73.38 %, and 71.38 %, respectively. Moreover, chemical activation methods were employed by Mbarki et al. (2022) to activate corn stigmata fibers using KOH, $ZnCl_2$, and H_3PO_4 reagents, resulting in three activated biochar samples with specific surface areas of 11, 389, and 589 m^2/g. Atinafu et al. (2018) synthesized biochar characterized by a large specific surface area and significant mesoporous ratio by utilizing dewaxed cotton as a precursor, then impregnating the cotton with MgO and carbonizing it at 700, 800, and 900 °C to prepare 1-hexadecanol composite PCMs. The specific surface areas of the activated biochar samples were 487.9, 717.7, and 876.6 m^2/g, respectively, with PCM loading capacities of 85 %, 90 %,

and 88 % for PCM.

In summary, chemically activated biochar exhibited superior textural characteristics and loading capacity compared with physically activated biochar. However, traditional chemical activation processes typically involve highly corrosive and toxic chemical activators that are hazardous to the environment. Some researchers have proposed using potassium salts, such as K_2CO_3, $KHCO_3$, and $K_2C_2O_4$, as alternative activators to produce activated biochar with high porosity while minimizing their adverse environmental impacts (Singh et al., 2023). Previous studies have reported the application of biochar activated by K_2CO_3 with specific surface areas ranging from 500 to 3000 m^2/g in supercapacitors (Demir and Doguscu, 2022; Mu et al., 2019), lithium-ion batteries (Arie et al., 2020; Ma et al., 2019; Xi et al., 2019), electrochemical hydrogen storage (Seifi et al., 2020), and other fields. The high porosity of biochar activated by K_2CO_3 makes it well-suited to PCM loading. However, there is a lack of relevant studies that have investigated the application of biochar activated by K_2CO_3 in PCM loading.

Therefore, in the current study, K_2CO_3 was utilized as a chemical activator, and various common biomass waste materials, including rice husk, bamboo, pine, walnut shell, and corncob, were employed as biomass precursors to produce five types of activated biochar for loading three commonly used organic PCMs (PA, stearic acid (SA), and polyethylene glycol (PEG)). Our investigation focused on the textural characteristics of synthetic biochar and its chemical compatibility with PCMs. Additionally, a comprehensive analysis was conducted to examine the effect of textural characteristics of biochar on the thermal properties of composite PCMs, as well as the effect of and the interaction between the biochar surface functional groups and different organic PCM molecules. Furthermore, the impact of activated biochar on the thermal conductivity and thermal stability of PCMs was also addressed. The purpose of this work is to explore the performance of biochar activated by K_2CO_3 derived from diverse biomass precursors in PCM loading and to assess its impact on PCM performance. Our intent is to enhance the performance and environmental sustainability of waste biomass-derived activated biochar in PCM loading applications.

2. Material and experimental approaches

2.1. Materials

All the reagents applied in this study were of analytical-grade purity and were employed without additional purification. Paraffin and K_2CO_3 (purity: 99 %) were obtained from Aladdin Chemistry Co. Ltd., and polyethylene glycol (average Mn: 6000) and HCl (AR, 36–38 %) were provided by Sinopharm Chemical Reagent Co. Ltd. Stearic acid (purity: 98 %) was provided by Shanghai Macklin Biochemical Technology Co. Ltd. The thermal properties of the PCMs employed in this work reported in previous studies are listed in Table 1.

2.2. Synthesis of activated biochar and activated biochar-based composite PCMs

Five common types of waste biomass, rice husk, bamboo, pine, walnut shell, and corncob, were obtained from local farms in Hangzhou, China, and used as precursors for the activated biochar. The preparation of activated biochar involved four main steps (Fig. 1): (1) The precursors were dried at 105 °C until a stable weight was reached and subsequently crushed before passing through a 0.5 mm sieve. The crushed precursors (250 g) and K_2CO_3 (500 g) were mixed in a beaker at a stoichiometric ratio of 1:2 (Kılıç et al., 2012; Mbarki et al., 2022). Subsequently, the mixture was subjected to agitation for 1 h to ensure homogeneity after 1000 mL of deionized water was added. (2) The mixture was left to impregnate at ambient temperature for 24 h, after which it was subjected to a 24-hour drying process at 105 °C to remove the water. (3) The dried mixture was then pyrolyzed in a vacuum muffle furnace whose diameter and length were 300 and 600 mm under a nitrogen atmosphere (5 L/min) at a heating rate of 10 °C/min. During the pyrolysis, a temperature of 700 °C was maintained for 2 h (Kwak et al., 2019; Wang et al., 2020). (4) The resulting sample was washed with a 10 % HCl solution and deionized water until the pH value reached 7 to ensure the removal of excess impurities. The prepared activated biochar was then heated at 105 °C for 24 h to obtain the final dried activated biochar. The activated biochar samples that were derived from rice husk, bamboo, pine, walnut shell, and corncob activated by K_2CO_3 were designated as RH, BB, PN, WS, and CC, respectively.

As illustrated in Fig. 1, the synthesis process comprised three primary steps: (1) A suitable amount of PCM (approximately 60 g) was weighed out and heated in a water bath at a temperature of 90 °C until it melted completely. Next, 10 g activated biochar was added to the liquid PCM under continuous stirring to ensure thorough mixing. Additional stirring was then conducted for 20 min to achieve a uniformly mixed combination of activated biochar and PCM. (2) The uniform mixture was transferred to a vacuum drying oven and heated for 24 h to allow the liquid PCM to fill the biochar pores under vacuum. (3) After the vacuum impregnation was complete, the mixture was transferred to filter paper and further processed in a 90 °C oven. The filter paper was replaced every 4 h to remove any leaked PCM liquid. When no significant PCM residue was observed on the filter paper, which took approximately 48 h, the shape-stable composite PCMs were considered to be successfully prepared. The composite PCM obtained by loading PA with RH was labeled PA/RH, and the remaining composite PCMs followed a similar naming convention.

2.3. Characterization

The textural characteristics of the activated biochar samples were characterized using a nitrogen sorption isotherm analyzer (ASAP 2460, Micromeritics) and the Brunauer-Emmett-Teller (BET) method. The textural characteristics were assessed using a relative pressure range of 0.05–0.15 at a temperature of 77 K. Field emission scanning electron microscope (SEM) (SU8010, HITACHI) characterized the microstructure of the synthetic samples. Fourier transform infrared (FT-IR) (Vertex 70, Bruker) evaluated the chemical compatibility between the biochar samples and PCM in the 500–4000 cm^{-1} wavenumber range. The thermal properties of the pure and composite PCM were determined utilizing a differential scanning calorimetry (DSC 25, TA) with an accuracy of ± 0.01 °C for temperature and ± 0.1 % for heat enthalpy. The measurement was performed under a constant N_2 flow rate of 50 mL/min. The thermal stability of the sample was assessed by employing a thermogravimetric (TG) analyzer (TGA 5500, TA) with an accuracy of ± 0.1 °C for temperature and ± 0.01 % for mass. The measurement was evaluated under a constant N_2 flow rate of 60 mL/min. The temperature range for the analysis was set from 25 °C to 600 °C, with a heating rate

Table 1
Thermal properties of the PCMs employed in this work.

Material	Peak melting temperature (°C)	Melting enthalpy (kJ/kg)	Peak solidification temperature (°C)	Solidification enthalpy (kJ/kg)	Reference
Paraffin	56.6	159.89	45.8	140.98	(Wang et al., 2023)
Stearic acid	71.52	219.45	65.84	218.54	(Chen et al., 2021)
Polyethylene glycol	63	189.6	38	–	(Lawag et al., 2023)

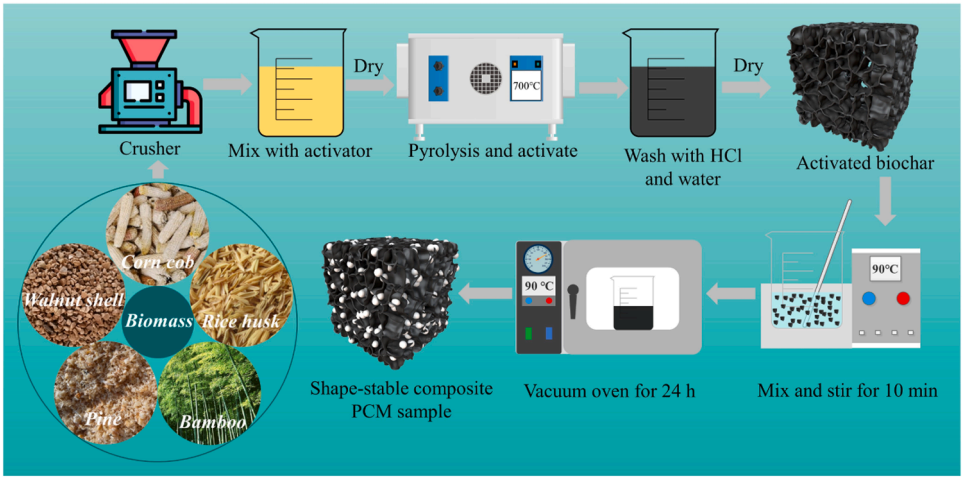

Fig. 1. Synthesis process for the activated biochar and composite PCMs.

of 10 °C/min. An X-ray diffractometer (X'pert Powder, PANalytical B.V.) equipped with Cu K-alpha radiation (k = 1.540598 Å) was utilized to obtain the X-ray diffraction (XRD) pattern of the activated biochar. The measurements were conducted in the range of 5–80°. The thermal conductivity of the activated biochar powder and the activated biochar-based composite PCMs was measured using a thermal constant analyzer (TCi, C-Therm) whose accuracy was ± 1 %.

3. Results and discussion

3.1. Textural characteristics

3.1.1. Textural characteristics of the activated biochar

The textural characteristics of the activated biochar samples RH, BB, PN, WS, and CC are illustrated in Fig. 2. Under the IUPAC classification of isotherms, these activated biochar samples all exhibited a pattern of type IV. These activated biochar samples exhibited a rapid increase in pore volume at low relative pressures, followed by a gradual upward trend (Fig. 2(a)), indicating the presence of numerous micropores and a smaller number of macropores (Lim et al., 2010). The substantial increase in nitrogen adsorption at lower relative pressures indicated the presence of numerous micropores in the activated biochar samples. As the relative pressure increased, the larger pores in the sample gradually became filled, resulting in a gradual increase in the adsorbed nitrogen amount, indicating a small number of mesopores. Furthermore, a distinct upward trend was observed at higher relative pressures, particularly in the RH samples, indicating the presence of macropores. This observation was further supported by the pore size distribution curves plotted in Fig. 2(b). Notably, the rate of pore volume increase for RH was significantly higher than that in other activated biochar samples at higher relative pressures, suggesting that RH possessed more macropores.

Table 2 presents the textural parameters and yield of the activated biochar samples synthesized in this work and the biochar reported in previous studies. The specific surface area (S_{BET}) of the biochar without activation was less than 50 m^2/g, while that of the activated biochar increased significantly after potassium carbonate activation. The

Table 2
Textural parameters and yield of the synthesis activated biochar in this work and the biochar reported in previous studies.

Biochar	S_{BET} (m^2/g)	V_{total} (cm^3/g)	$D_{average}$ (nm)	Y (%)[a]	References
Phoenix leaf	14.18	0.024	8.707	39.45	(Lv et al., 2022)
Pristine wood	3.9	0.13	–	–	(Yang et al., 2018)
Empty fruit bunch	4.1	–	7.1	33.0	(Yek et al., 2021)
RH	753.60	0.434	8.995	24.14	This work
BB	845.61	0.389	5.061	26.11	This work
PN	849.64	0.377	4.013	26.02	This work
WS	994.88	0.456	4.488	26.21	This work
CC	1053.95	0.467	4.208	26.15	This work

[a] Uncertainty: ± 0.006 %.

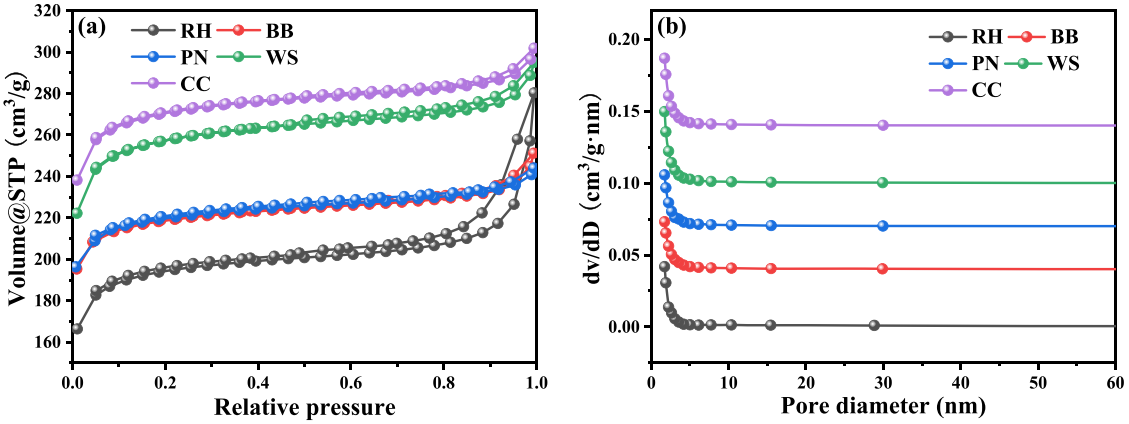

Fig. 2. (a) Nitrogen sorption-desorption isotherms, and (b) pore size distribution of the activated biochar samples RH, BB, PN, WS, and CC.

activated biochar CC exhibited the highest S_{BET} of 1053.95 m^2/g, followed by those of WS, PN, BB, and RH at 994.88, 849.64, 845.61, and 753.60 m^2/g, respectively. Moreover, the total pore volume (V_{total}) of the biochar without activation was also much smaller than that of the activated biochar. CC showed the highest V_{total} of 0.467 cm^3/g, whereas WS, PN, BB, and RH had values of 0.456, 0.377, 0.389, and 0.434 cm^3/g, respectively. The critical textural characteristic of activated biochar lies in its elevated specific surface area and adjustable pore size distribution. A greater specific surface area enables more surface functional groups, enhancing the contact area between activated biochar and PCM and reinforcing the interaction between functional groups and PCM. Moreover, a larger total pore volume signifies an augmented presence of internal pores, which provides additional space for PCM accommodation. Consequently, larger S_{BET} and V_{total} of activated biochar lead to increased loading of PCM.

These differences in S_{BET} and V_{total} may have resulted from the distribution of micropores and macropores in various activated biochar samples. Notably, despite having the smallest specific surface area, RH exhibited a larger pore volume than PN and BB, mainly due to its higher proportion of macropores. The above phenomenon was further demonstrated by the average pore size ($D_{average}$) of the activated biochar, where PN had the smallest average pore size, followed by CC, WS, BB, and RH. The variations in textural characteristics between the activated biochar samples can be attributed to the carbon composition of the biomass precursors and the differences in the three main components (cellulose, hemicellulose, and lignin) (Gayathiri et al., 2022). Additionally, the yield (Y) of the activated biochar samples was obtained utilizing the following equation:

$$Y = \frac{W_{AB}}{W_{precursor}} \quad (1)$$

where $W_{precursor}$ and W_{AB} represent the masses of the biomass precursor and the biochar activated by K_2CO_3, respectively. The differences in yield between the various activated biochar samples were insignificant. Of the samples, the activated biochar RH had the lowest yield of 24.14 %; this can be attributed to the elimination of more non-carbon elements in the rice husk precursor at high temperatures, consistent with a higher proportion of macropores in RH.

3.1.2. Surface microstructure of the activated biochar

The SEM images of the activated biochar samples RH, BB, PN, WS, and CC are displayed in Fig. 3. The surface microstructure of the activated biochar samples prepared utilizing different precursors activated by K_2CO_3 exhibited remarkable similarities, characterized by the presence of well-developed pores and highly porous structures. These SEM images revealed a multitude of small pores and channels, depicting a diverse multi-level pore structure. These pores exhibited irregular shapes with a relatively uniform size distribution. Furthermore, the interconnected pores formed a complex and interconnected network. This structural feature confirmed the activated biochar's substantial specific surface area and total pore volume resulting from the activation process using K_2CO_3. Additionally, the activated biochar sample surface displayed intricate textures and microscopic features, indicating the abundant presence of functional groups. These images reveal the formation of highly porous structures of varying sizes in different activated biochar samples and indicate the development of a high-porosity carbon matrix. These collective characteristics contributed to the activated biochar's exceptional adsorption capacity and ample loading capacity for PCM. The formation of a porous texture in activated biochar can be attributed to the impregnation and activation mechanisms that involve K_2CO_3 (Singh et al., 2023). $KHCO_3$ was generated when the biomass precursors were impregnated with K_2CO_3 during the impregnation process. At high temperatures, the non-carbon elements of the precursors decomposed, leading to the condensation of carbon into aromatic frameworks. Subsequently, $KHCO_3$ underwent conversion to K_2CO_3, H_2O, and CO_2 at temperatures below 200 °C. These compounds then reacted with carbon and etched the aromatic skeleton at higher temperatures to form the porous texture.

$$2KHCO_3 \rightarrow K_2CO_3 + H_2O + CO_2 \quad (2)$$

$$K_2CO_3 + 2\,C \rightarrow 2\,K + 3CO \quad (3)$$

$$H_2O + CO_2 + 2\,C \rightarrow H_2 + 3CO \quad (4)$$

3.1.3. Surface microstructure of the composite PCMs

The SEM images of PA, SA, PEG/RH, BB, PN, WS, and CC composite PCMs, which show the loading of three organic PCMs by the activated biochar prepared with various precursors, are exhibited in Fig. 4. All the prepared composite PCMs exhibited a uniform PCM distribution, and their surface morphology was denser than that of the supporting activated biochar supporting material. Only a small amount of activated biochar pores on their surface were not filled with PCM (as shown in Fig. 4(a, f, m)). Therefore, the activated biochar effectively loaded three

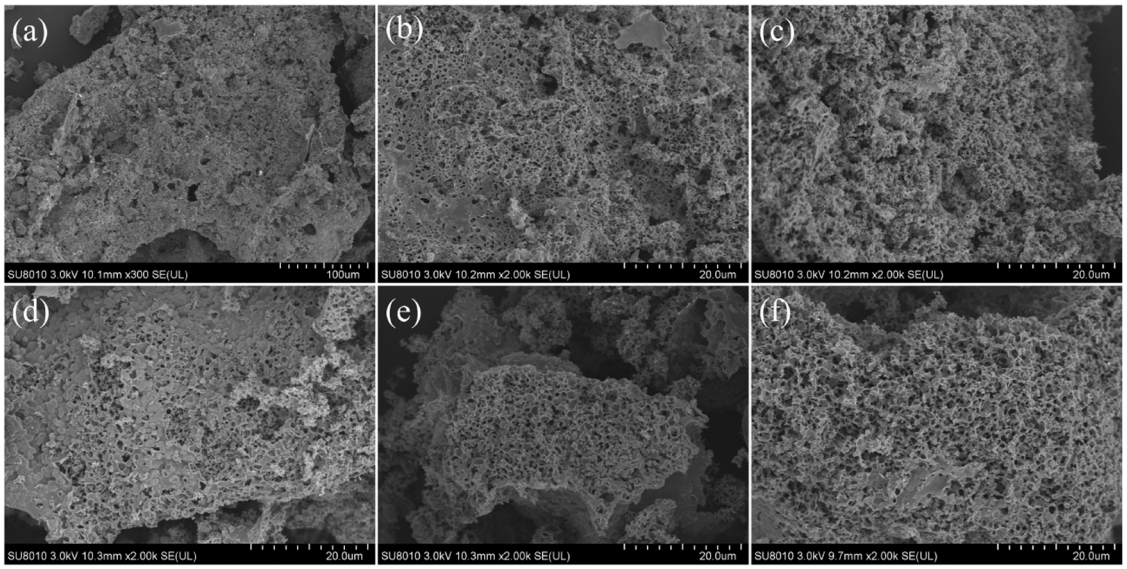

Fig. 3. SEM images of activated biochar: (a) RH (100 μm), (b) RH (20 μm), (c) BB, (d) PN, (e) WS, and (f) CC.

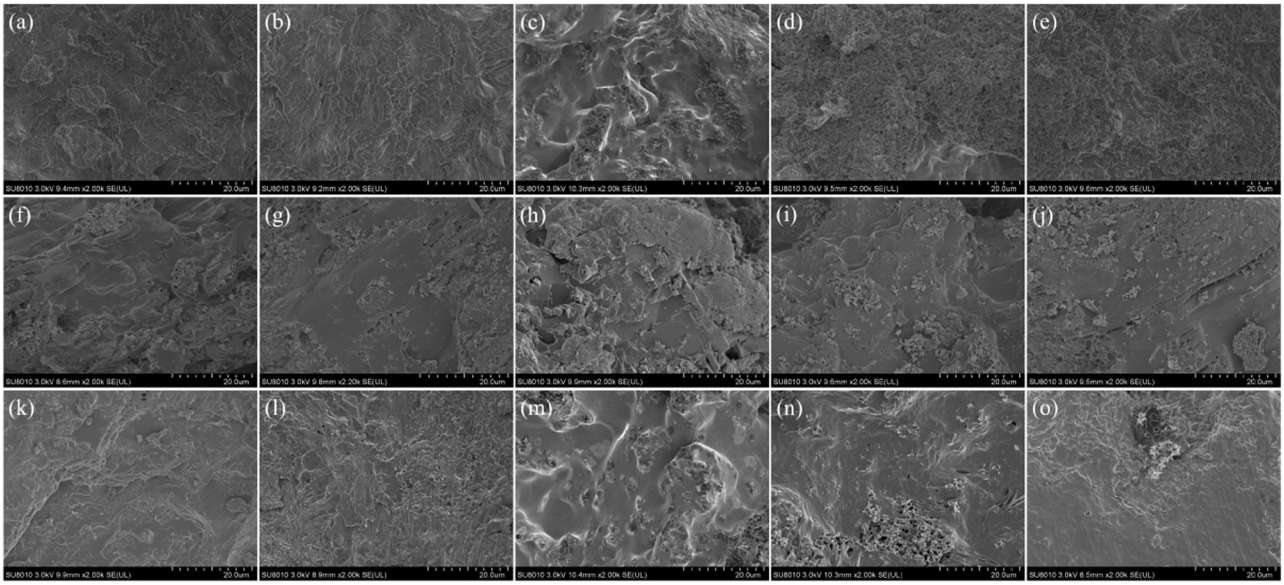

Fig. 4. SEM images of (a–e) PA, (f–j) SA, (k–o) PEG/RH, BB, PN, WS, and CC composite PCMs.

organic PCMs through capillary force and surface tension.

3.2. Chemical compatibility

Fig. 5(a) and Table S1 compare the FT-IR spectra of various activated biochar samples. The biochar samples exhibited a wide and intense absorption peak in the 3432–3446 cm^{-1} range, which corresponded to the stretching vibration of –OH groups (Cao et al., 2018). The absorption peak for the 2923–2929 cm^{-1} wavenumber may be ascribed to the asymmetric stretching of fatty $–CH_2$ groups and the stretching vibration of symmetrical C–H bonds (B et al., 2008). An IR absorption band was observed in the range of 1614–1620 cm^{-1}, suggesting a distinct type of shear vibration within the aromatic ring framework or a bending vibration of C═O, which is related to the overall vibration that results from water adsorption by the material (Ausavasukhi et al., 2016). The IR absorption band located at 1092–1186 cm^{-1} may be assigned to the association of O–H groups and C–O axial deformation in carboxyl acids, aromatic esters, and aliphatic and aromatic ethers (Zhao et al., 2013).

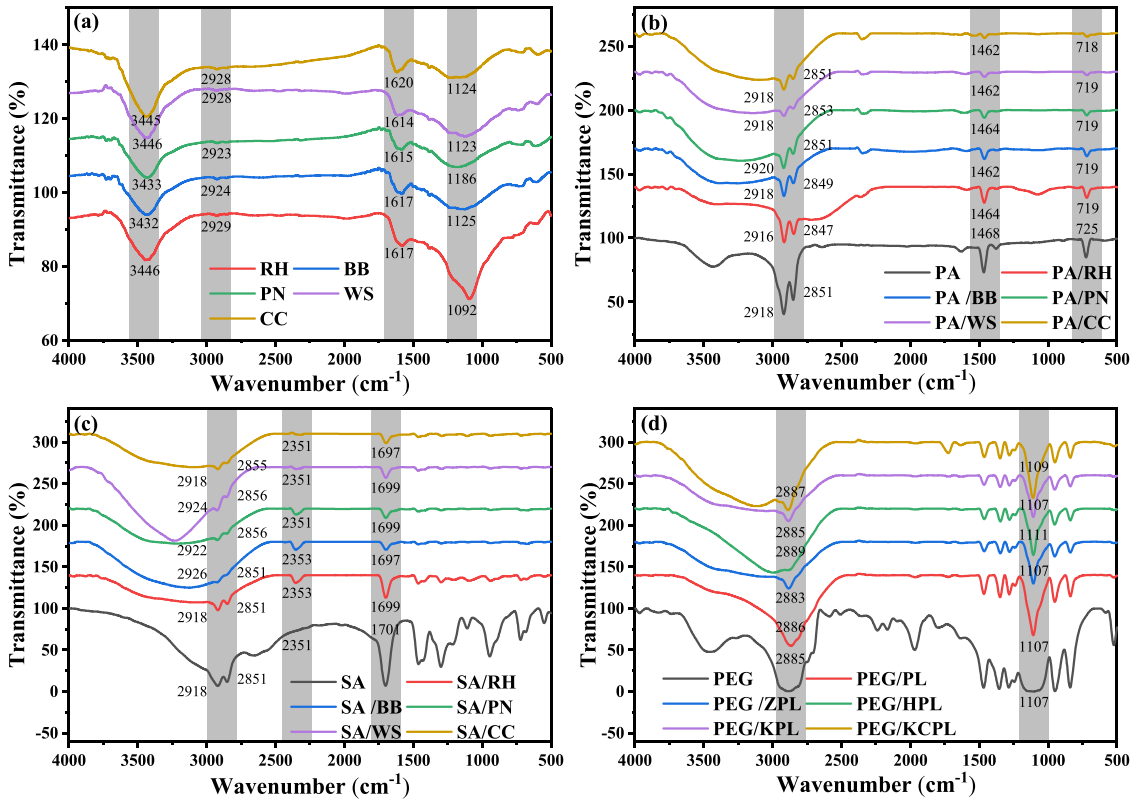

Fig. 5. FT-IR spectra of (a) activated biochar samples prepared using various precursors, (b) PA and PA/RH, BB, PN, WS, and CC composite PCMs, (c) SA and SA/RH, BB, PN, WS, and CC composite PCMs, (d) PEG, PEG/RH, BB, PN, WS, and CC composite PCMs.

Some changes and displacements were found for the activated biochar sample prepared using various precursors, and these changes might have been due to the difference in the composition of cellulose, hemicellulose, and lignin in different biomass precursors.

The IR absorption bands of the composite PCMs exhibited remarkable similarity to those of the pure PCMs (Fig. 5(b–d)), albeit with a noticeable decrease in intensity. Additionally, the introduction of activated biochar support materials led to the enhancement of certain characteristic peaks in the IR absorption band of the composite PCMs, although these peaks were not pronounced. This can be attributed to the comparatively low proportion of support material within the composite PCMs, thus indicating the excellent chemical compatibility between the activated biochar and the PCMs.

Furthermore, the potential physical and chemical interactions between activated biochar and PCM were addressed. Previous studies have reported several interactions between activated biochar and PCM, including pore-filling (Luo et al., 2022), hydrogen-bonding (Atinafu et al., 2021b), hydrophobic interaction, and other possible mechanisms (Lv et al., 2022), as illustrated in Fig. 6. Firstly, the nitrogen- and oxygen-containing functional groups on the activated biochar surface can facilitate the filling of PCM into the pores through intermolecular interactions. Secondly, the hydrogen-bonding can further enhance the loading capacity of PCM. Lastly, hydrophobic interaction, along with other potential interactions, can influence the loading behavior of activated biochar on PCM. It is noteworthy that the interaction between activated biochar and PCM molecules may also impact the melting and solidification processes of PCM inside activated biochar, thereby affecting their thermal properties in addition to increasing the PCM loading. The influence of the activated biochar-PCM interactions on the thermal performance of PCM will be extensively discussed in Section 3.3.

3.3. Thermal properties

3.3.1. Phase transition temperature and enthalpy

Fig. 7(a–c) presents the DSC endothermic and exothermic curves of three PCMs and the corresponding composite PCMs. Introducing activated biochar into PCM did not cause significant changes in the DSC curve, indicating good chemical compatibility between the PCM and the biochar. However, noticeable shifts in position and intensity were observed in the DSC curves. Fig. 7(d) and Table 3 provide a comparison of the peak melting temperature (T_m) and peak solidification temperature (T_s) of the pure and the composite PCM samples. The addition of activated biochar slightly decreased the T_m and T_s of the composite PCMs. For instance, the incorporation of activated biochar led to a decrease in the T_m and T_s of PA. The T_m and T_s values of PA were reduced from 57.73/55.19 °C to 56.83/53.20, 57.04/53.25, 56.09/52.05, 57.16/52.86, and 57.11/52.94 °C for PA/RH, PA/BB, PA/PN, PA/WS, and PA/CC, respectively. Similarly, comparable findings were observed in the SA and PEG composite PCM. The decrease in peak melting and solidification temperatures of PCM, following the addition of activated biochar, could be attributed to the textural characteristics of biochar and various interactions between the surface functional groups of the biochar and different PCM molecules (Atinafu et al., 2020b).

Fig. 8(a) illustrates the endothermic and exothermic heat enthalpies (ΔH_{endo} and ΔH_{exo}) of the pure and the composite PCM samples. After the introduction of activated biochar, the endothermic enthalpy of PA decreased from 225.24 kJ/kg to 156.06, 151.55, 151.46, 156.31, and 152.38 kJ/kg for PA/RH, PA/BB, PA/PN, PA/WS, and PA/CC. Similarly, the endothermic enthalpy of SA decreased from 231.87 kJ/kg to 162.09, 158.96, 170.63, 168.88, and 175.27 kJ/kg for SA/RH, SA/BB, SA/PN, SA/WS, and SA/CC, whereas that of PEG decreased from 188.79 kJ/kg to 130.45, 133.94, 137.39, 119.03, and 121.94 kJ/kg for PEG/RH, PEG/BB, PEG/PN, PEG/WS, and PEG/CC. The exothermic enthalpies of the composite PCMs followed a trend similar to those of the endothermic enthalpies, so it will not be elaborated here. There are three main reasons for the decrease in endothermic and exothermic enthalpies of the composite PCM samples. (1) The introduced activated biochar material accounted for a certain proportion of weight in the composite PCMs and did not undergo phase transition within the temperature range tested by DSC. (2) Some PCMs might not have undergone phase change during endothermic and exothermic processes due to the capillary force and surface tension in the smaller pores of the activated biochar. (3) The interaction between the surface functional groups of the activated biochar and the PCM molecules prevented the phase transition of the PCM that was in contact with the biochar surface.

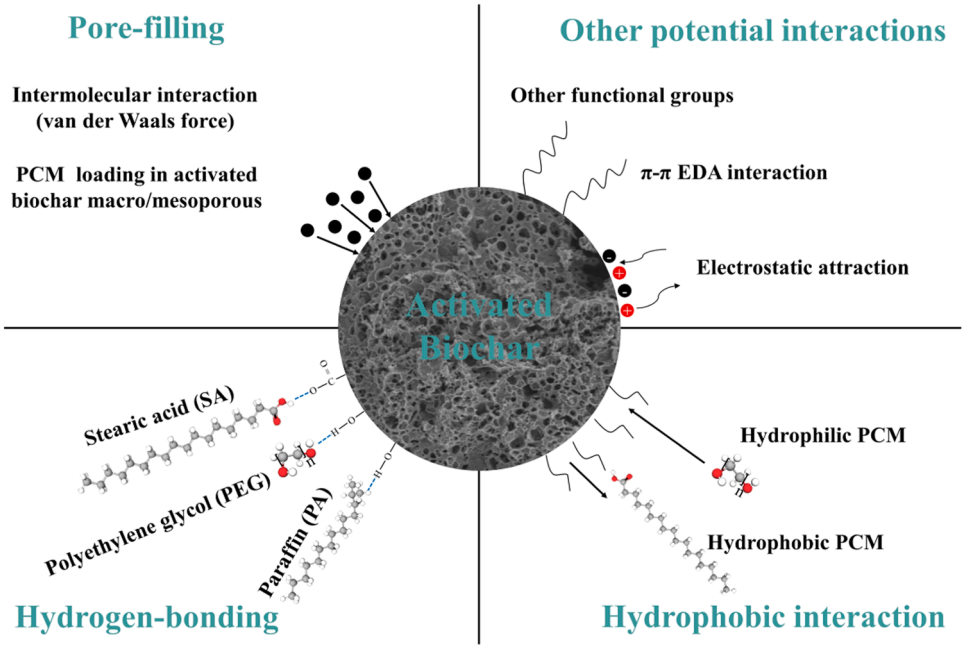

Fig. 6. Potential physical and chemical interactions between activated biochar and organic PCM.

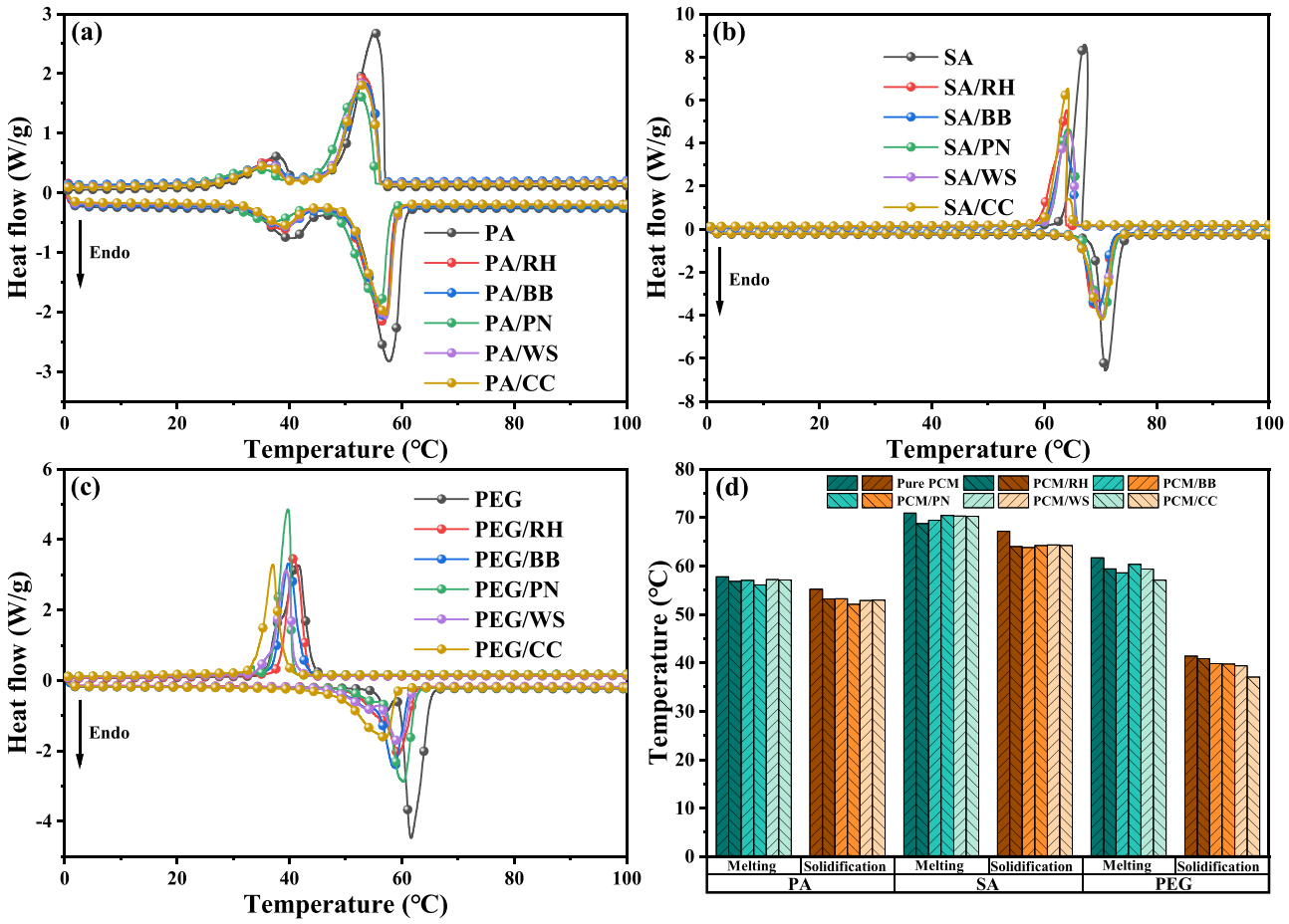

Fig. 7. DSC curves of (a) PA, (b) SA, and (c) PEG composite PCM samples, and (d) peak melting temperature and peak solidification temperature of pure and composite PCM samples.

3.3.2. *Loading capacity and loading efficiency*

The loading capacity *C* was proposed to evaluate the effect of the weight proportion of the activated biochar on the endothermic and exothermic enthalpies of the composite PCMs, and the loading efficiency *E* (Li et al., 2013) was used to assess the impact on the enthalpy of the textural characteristics and the surface functional group interactions of the introduced biochar. The following Eqs. (5 and 6) calculate the loading capacity and the loading efficiency:

$$C = \frac{m_{CPCM} - m_{AB}}{m_{CPCM}} \tag{5}$$

$$E = \frac{\Delta H_{endo,CPCM} + \Delta H_{exo,CPCM}}{\Delta H_{endo,PCM} + \Delta H_{exo,PCM}} \tag{6}$$

where m_{CPCM} and m_{AB} are the mass of the composite PCMs and the mass of the activated biochar in the composite PCMs; $\Delta H_{endo,CPCM}$, $\Delta H_{exo,CPCM}$, $\Delta H_{endo,PCM}$ and $\Delta H_{exo,PCM}$ refer to the endothermic and exothermic enthalpies of the composite PCM and the pure PCM, respectively.

A comparison of the values of *C* and *E* of the activated biochar for PA, SA, and PEG is depicted in Fig. 8(b) and summarized in Table 3. The loading capacities for RH, BB, PN, WS, and CC for PA were 78.80 %, 78.47 %, 81.12 %, 78.16 %, and 78.79 %, respectively. Their loading capacities for SA were 80.35 %, 79.38 %, 82.89 %, 78.45 %, and 80.83 %, respectively, and their loading capacities for PEG were 84.7 %, 82.86 %, 85.08 %, 83.47 %, and 85.19 %, respectively. The activated biochar exhibited the highest loading capacity for PEG, followed by its loading capacity for SA and PA. The difference between the PCMs could be attributed to their varying functional groups and their interactions with the surface functional groups of the activated biochar, which ultimately influenced the loading capacity. Of the types of activated biochar, PN demonstrated the highest loading capacity for all three organic PCMs. However, the differences between the other activated biochar samples were insignificant. This observation may be attributed to PN having the smallest average diameter, which provides enhanced capillary force and surface tension and thereby facilitates a more favorable environment for PCM loading. The loading capacities of the activated biochar for organic PCMs reported in other work are listed in Table 4. The activated biochar obtained by treating different biomass precursors with K_2CO_3 demonstrated a better loading capacity for the three types of organic PCMs than most biochar prepared using alternative methods or activators. Meanwhile, the composite PCMs prepared using K_2CO_3 exhibited more appealing endothermic and exothermic enthalpies.

Considering the impact of their textural characteristics and surface functional group interactions on the enthalpies of the composite PCMs, the loading efficiencies of the biochar samples were lower than their corresponding loading capacities, as shown in Fig. 8(b) and listed in Table 3. Activated biochar seemed to have the highest loading efficiency for SA, followed by its efficiencies for PA and PEG, which could be attributed to the differential interactions between the activated biochar and organic PCMs, which had different functional groups and varying molecular sizes. The differences in the interactions could be further obtained by the influence degree η proposed in our previous work (Lv et al., 2022).

$$\eta = \left(1 - \frac{E}{C}\right) \times 100\% \tag{7}$$

Overall, the textural characteristics and surface functional groups of

Table 3
Thermal properties of pure and composite PCMs, loading capacity (*C*), loading efficiency (*E*), and influence degree (η) of activated biochar on PCMs. ΔH_{endo} and ΔH_{exo} are the heat enthalpies of the sample in the endothermic and exothermic processes, respectively.

Sample	T_m (°C)	ΔH_{endo} (kJ/kg)	T_s (°C)	ΔH_{exo} (kJ/kg)	*C* (%)	*E* (%)	η (%)
PA	57.73	225.24	55.19	227.13	–	–	–
PA/RH	56.83	156.06	53.20	159.98	78.80 ± 0.03	69.86 ± 0.11	11.34 ± 0.14
PA/BB	57.04	151.55	53.25	152.86	78.47 ± 0.03	67.29 ± 0.10	14.24 ± 0.13
PA/PN	56.09	151.46	52.05	153.23	81.12 ± 0.03	67.35 ± 0.10	16.97 ± 0.13
PA/WS	57.16	156.31	52.86	158.12	78.16 ± 0.03	69.51 ± 0.10	11.07 ± 0.14
PA/CC	57.11	152.38	52.94	154.37	78.79 ± 0.03	67.81 ± 0.10	13.94 ± 0.13
SA	70.87	231.87	67.17	231.98	–	–	–
SA/RH	68.73	162.09	64.00	160.74	80.35 ± 0.03	69.60 ± 0.10	13.38 ± 0.13
SA/BB	69.44	158.96	63.82	158.77	79.38 ± 0.03	68.50 ± 0.10	13.71 ± 0.13
SA/PN	70.41	170.63	64.21	168.53	82.89 ± 0.03	73.12 ± 0.11	11.79 ± 0.13
SA/WS	70.30	168.88	64.32	165.35	78.45 ± 0.03	72.06 ± 0.11	8.15 ± 0.14
SA/CC	70.27	175.27	64.19	176.70	80.83 ± 0.03	75.88 ± 0.11	6.12 ± 0.14
PEG	61.67	188.79	41.36	182.85	–	–	–
PEG/RH	59.37	130.45	40.81	126.96	84.70 ± 0.02	69.26 ± 0.11	18.23 ± 0.13
PEG/BB	58.56	133.94	39.81	128.52	82.86 ± 0.03	70.62 ± 0.11	14.77 ± 0.14
PEG/PN	60.30	137.39	39.74	135.70	85.07 ± 0.02	73.48 ± 0.12	13.62 ± 0.14
PEG/WS	59.35	119.03	39.37	113.97	83.46 ± 0.02	62.70 ± 0.10	24.88 ± 0.12
PEG/CC	57.05	121.94	37.06	118.92	85.19 ± 0.02	64.81 ± 0.10	23.92 ± 0.12

the activated biochar exhibited the greatest influence degree on the endothermic and exothermic enthalpies of PEG, followed by their influence degree on PA and SA, which aligned with the results for loading efficiency. For instance, the influence degree of WS on PEG was as high as 24.88 %, while that on PA and SA decreased to 11.07 % and 8.15 %, respectively. However, there was no distinct pattern regarding the influence degree of different activated biochar samples on the PCMs. This could be attributed to variations in specific surface area, average pore size, and surface functional groups of the activated biochar.

Furthermore, the loading capacity and influence degree of the biochar activated by K_2CO_3 on organic PCMs were compared with that of other carbon materials reported in previous studies, such as EG, CNT, graphene, and physically activated biochar. It was observed that the loading capacity of the biochar activated using K_2CO_3 for organic PCMs was comparable to that of other carbon support materials with good performance, whereas its influence degree on PCMs was relatively low. This further supports the suitability of the activated biochar prepared using K_2CO_3 for loading organic PCMs and offers a promising option for the future utilization of discarded biomass biochar in PCM loading.

3.4. Thermal conductivity

First, the thermal conductivity of different activated biochar powders was measured, as depicted in Fig. 9(a). Of the activated biochar powders, RH exhibited the highest thermal conductivity of 0.06 W/(m·K), followed by WS, BB, CC, and PN, which had values of 0.059, 0.057, 0.054, and 0.051 W/(m·K). The variations in thermal conductivity of these activated biochar samples can be explained by the arrangement of the carbon sheets in single layers, which can be quantified by the ratio *R* of the height of the Bragg peak to the background (Wang et al., 2009). A higher *R* corresponds to greater thermal conductivity.

The thermal conductivity values of PA, SA, and PEG, as well as their corresponding composite PCMs, are presented in Fig. 9(c). The result indicates that introducing activated biochar enhanced the thermal conductivity of the three PCM types to different extents, with RH demonstrating the most significant improvement in thermal conductivity, followed by WS, BB, CC, and PN. For example, the thermal conductivity of PA/RH, PA/BB, PA/PN, PA/WS, and PA/CC increased from an initial value of 0.302 W/(m·K) for pure PA to 0.441, 0.414, 0.405, 0.421, and 0.411 W/(m·K), respectively, which corresponded to increases of 1.46-, 1.37-, 1.34-, 1.39-, and 1.36-fold. The observed variations in the thermal conductivity improvement between the different activated biochar samples can be attributed to disparities in the thermal conductivity of the biochar itself, as activated biochar samples that were prepared using different precursors exhibited distinct thermal conductivities (Kim et al., 2021; Yang et al., 2019). The composite PCM added with activated biochar with higher thermal conductivity also possessed higher thermal conductivity.

3.5. Thermal stability

The TG curve of the PA composite PCMs exhibited a notable backward shift upon the addition of activated biochar, as shown in Fig. 10(b). The peak decomposition temperature was increased from 264.76 °C for pure PA to 286.63, 283.31, 287.33, 286.66, and 286.91 °C for PA/RH, PA/BB, PA/PN, PA/WS, and PA/CC, respectively. For SA, no significant change was observed in the TG curve or the peak decomposition temperature of its composite PCMs (Fig. 10(d)). For PEG, the TG curve of its composite PCMs also demonstrated a significant backward shift upon mixing with biochar, and the peak decomposition temperature was increased from 369.00 °C for pure PEG to 375.60, 377.24, 372.42, 372.90, and 372.11 °C for PEG/RH, PEG/BB, PEG/PN, PEG/WS, and PEG/CC, respectively (Fig. 10(f)). In summary, incorporating organic PCMs into activated biochar increased the peak decomposition temperature, which indicated an enhancement of the thermal stability of the composite PCMs. Activated biochar exhibited the highest enhancement in the thermal stability of PA, followed by its enhancement in PEG and SA. This phenomenon could be attributed to the interactions between the activated biochar and the organic PCMs, which had different functional groups and molecular sizes. Similar results have been reported in previous research (Atinafu et al., 2021a; Das et al., 2020; Gao et al., 2021).

Furthermore, the DTG curves of the composite PCMs displayed a single prominent peak, corresponding to the decomposition of the PCMs in the composite. No decomposition peak of the activated biochar component was observed in the DTG curve. This absence can be attributed to the synthesis conditions of the activated biochar, which was synthesized at a high temperature of 700 °C in a vacuum muffle furnace. In contrast, the TG testing temperature range in this study was limited to a maximum of 600 °C, which was lower than the synthesis temperature. Consequently, the activated biochar component did not undergo decomposition within the temperature range covered by the TG testing, aligning with findings reported in previous studies (Atinafu et al., 2020a; Das et al., 2020).

Fig. 11 displays photographs of PA, SA, and PEG composite PCMs subject to drying in a 90 °C oven for 30 min. Notably, no obvious leakage of liquid PCM was observed in these composite PCMs after the heating process, signifying the successful fabrication of shape-stable composite PCMs. This observation further suggested that the biochar's high specific surface area and small pore size contributed to the capillary forces, surface tension, and interaction energy between the surface functional groups. These factors effectively confined the organic PCM within the microstructure of the activated biochar.

Finally, a 100 thermal cycles test was conducted to assess the thermal stability and reliability of PA/PN, SA/PN, and PEG/PN composite PCMs.

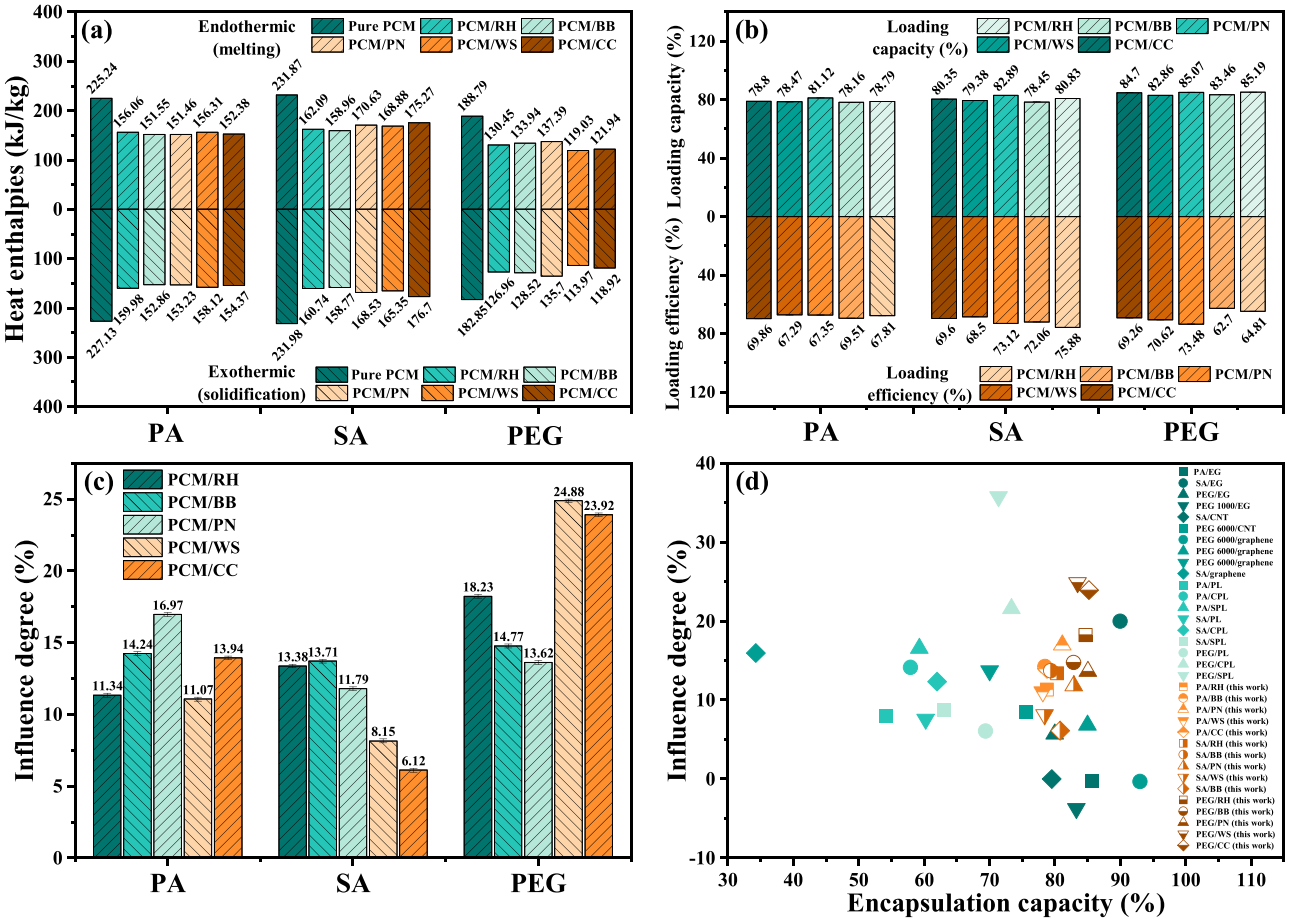

Fig. 8. (a) Endothermic and exothermic enthalpies of pure and composite PCM samples, (b) loading capacity and loading efficiency of various activated types of biochar for PCMs, (c) influence degree of various types of activated biochar on PCMs, and (d) comparison of influence degree of biochar on PCMs reported in other work and this work.

Table 4
Thermal properties of reported biochar-based composite PCMs.

Activated biochar	PCM	Melting temperature (°C)	Loading capacity (%)	Fusion enthalpy (kJ/kg)	Enhancement of thermal conductivity	References
Softwood	n-eicosane	37.0	26.4	52	–	(Atinafu et al., 2021b)
Oilseed rape	1-dodecanol	21.9	38.4	73.7	–	(Atinafu et al., 2020b)
	n-dodecane	–4.1	60.2	90.5	–	(Atinafu et al., 2020b)
Rice husk	Paraffin	48.2	70.1	95.7	1.77	(Yu et al., 2021)
Succulents-based carbon aerogel	Paraffin	53.3	95	115.2	–	(Wei et al., 2018b)
Hemp shives	Capric acid	28.9	55.93	78.7	1.26	(Sawadogo et al., 2022)
Abandoned rice	Palmitic-lauric acid	34.3	78.8	135.4	1.83	(Zhang et al., 2017)
Pinecone	Palmitic acid	59.25	60	84.74	1.44	(Wan et al., 2019)
Cabbage mustard	Tetra decanoic acid	50.6	57.07	103.55	2.18	(Gao et al., 2021)
Towel gourd	PEG 2000	59.6	94.5	164.3	–	(Song et al., 2020)
Pomelo peel flour	PEG-6000	60	78.55	143.2	–	(Hai-Chen et al., 2019)
Almond shell	PEG 4000	62.76	60	82.73	1.60	(Chen et al., 2018)
Potatoes	PEG 4000	56.67	50	91.80	–	(Tan et al., 2016)
Watermelon rind	Mannitol	170.22	87.5	262.6	1.68	(Liu et al., 2021a)
Watermelon rind	Sodium acetate trihydrate	63.2	–	210	1.85	(Liu et al., 2021b)

The results, presented in Fig. 12, indicated that the peak melting/solidification temperatures of PA/PN, SA/PN, and PEG/PN increased from their initial values of 56.09/52.05, 70.41/64.21, and 60.30/39.74 °C to 56.47/51.33, 70.72/64.78, and 60.98/40.65 °C, respectively, after the test. Furthermore, the endothermic and exothermic enthalpies of PA/PN, SA/PN, and PEG/PN decreased from 151.46/153.23, 170.63/

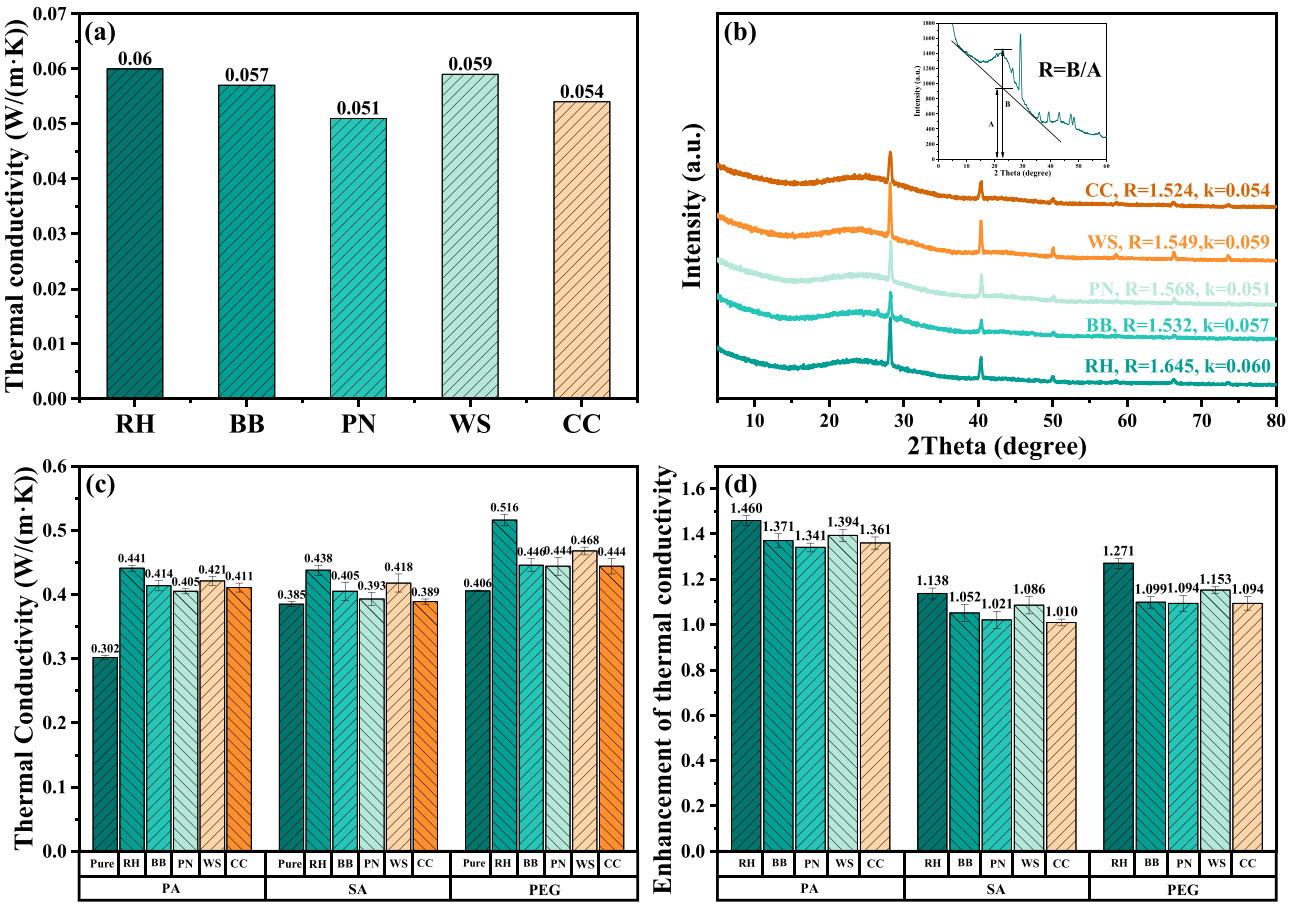

Fig. 9. (a) Thermal conductivity of pure and composite PCMs, (b) thermal conductivity enhancement of activated biochar on PCMs, (c) thermal conductivity of activated biochar powder, and (d) XRD patterns of activated biochar samples.

168.53, and 137.39/135.70 kJ/kg to 150.91/153.34, 169.90/168.35, and 137.12/135.05 kJ/kg, respectively. These marginal changes in melting and solidification temperature and enthalpies prior to and following the thermal cyclic test demonstrated the excellent cycling stability of the composite PCMs.

4. Conclusion

This study utilized environmentally friendly K_2CO_3 as an activator in the preparation of five types of activated biochar using discarded biomass, including rice husk, bamboo, pine, walnut shell, and corncob as precursors. Subsequently, five types of biochar were employed to load three common organic PCMs, PA, SA, and PEG, to investigate the impact of activated biochar on the thermal performance of the PCMs. The textural characteristics of the activated biochar and the surface microstructure, chemical compatibility, thermal properties, and thermal conductivity of the composite PCMs were studied. The primary findings derived from this study are summarized as follows:

(1) The biochar activated with K_2CO_3 had a rich pore structure, attractive specific surface area, and large total pore volume. The specific surface area and total pore volume of the activated biochar CC were as high as 1053.95 m^2/g and 0.467 cm^3/g, respectively.
(2) The activated biochar prepared using different precursors effectively loaded three organic PCMs through capillary force and surface tension and showed good chemical compatibility.
(3) The large specific surface area, rich textural characteristics, and surface functional groups of activated biochar enhanced the interaction between the activated biochar and the organic PCMs, which effectively improved the loading capacity while reducing loading efficiency and led to a higher influence degree. The loading capacities of CC for PA, SA, and PEG were as high as 78.79 %, 80.83 %, and 85.19 %, respectively, with corresponding influence degrees of 13.94 %, 6.12 %, and 23.92 %.
(4) Introducing activated biochar into organic PCMs enhanced their thermal conductivity effectively. RH demonstrated the most significant thermal conductivity improvement for the PCMs, followed by WS, BB, CC, and PN. The thermal conductivity values of the composites PA/RH, SA/RH, and PEG/RH were 1.460, 1.138, and 1.271 times that of the pure PCMs.
(5) After the activated biochar was introduced, the thermal stability of composite PCMs was significantly improved. The activated biochar demonstrated the greatest improvement in the thermal stability of PA, followed by PEG and SA. The thermal cycling test demonstrated the excellent cycling stability of the composite PCMs.

Therefore, the environmentally friendly activated biochar obtained by activating various biomass precursors with potassium carbonate exhibited a substantial specific surface area and a diverse pore structure. The activated biochar demonstrated a remarkable loading capacity of up to 80 % for organic PCMs, resulting in composite PCMs with excellent thermal stability, significant heat enthalpy, and enhanced thermal conductivity. These composite PCMs have extensive applications in domestic hot water production and the thermal management of electronic components.

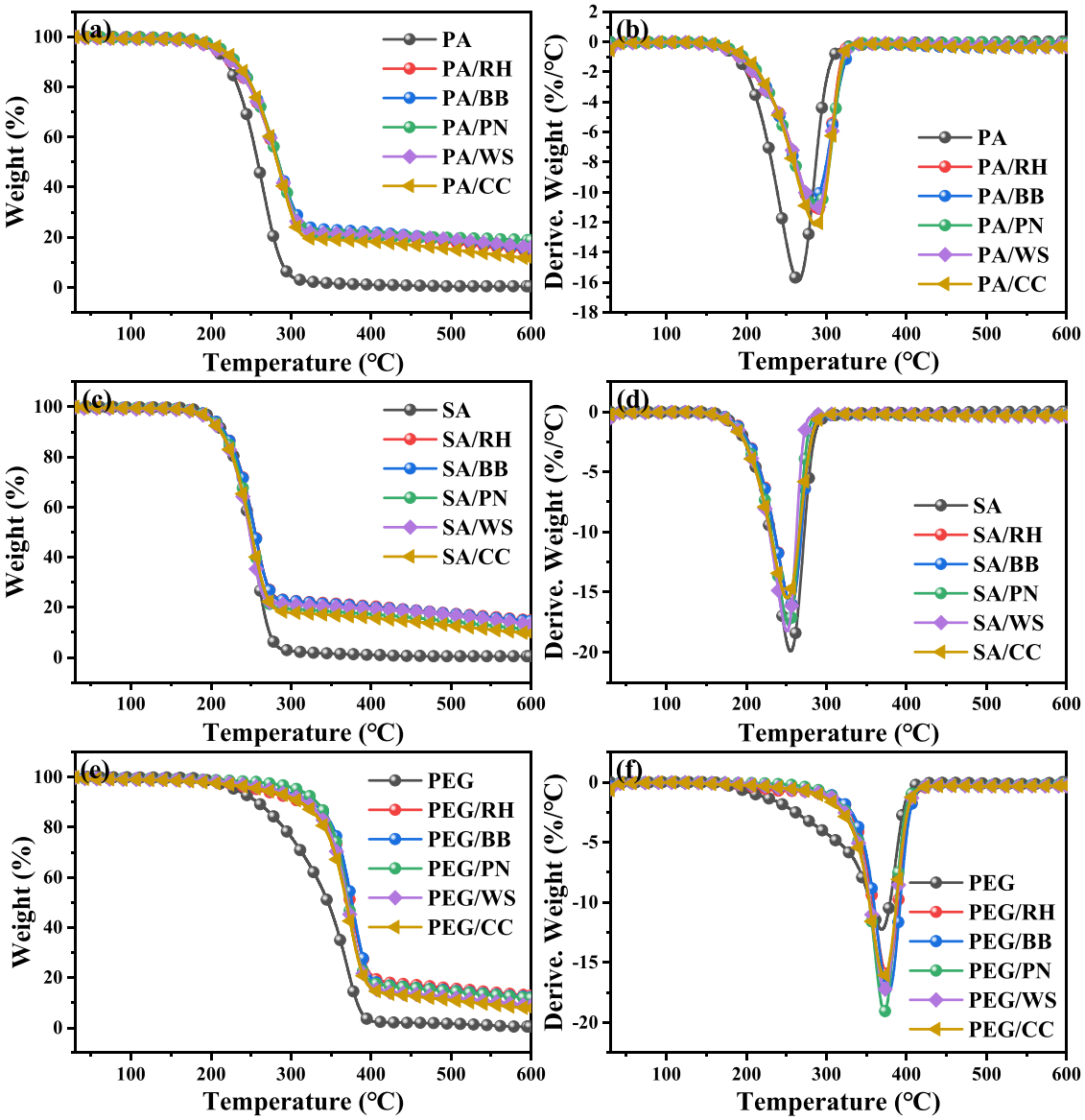

Fig. 10. TG and DTG curves for (a, b) PA, (c, d) SA, (e, f) PEG composite PCMs.

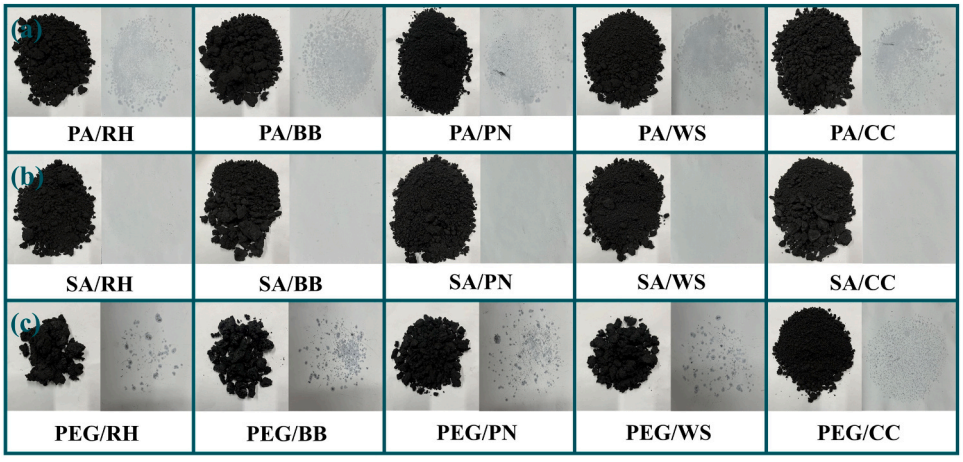

Fig. 11. Photographs of (a) PA, (b) SA, and (c) PEG composite PCMs subject to drying at 90 °C for 30 min.

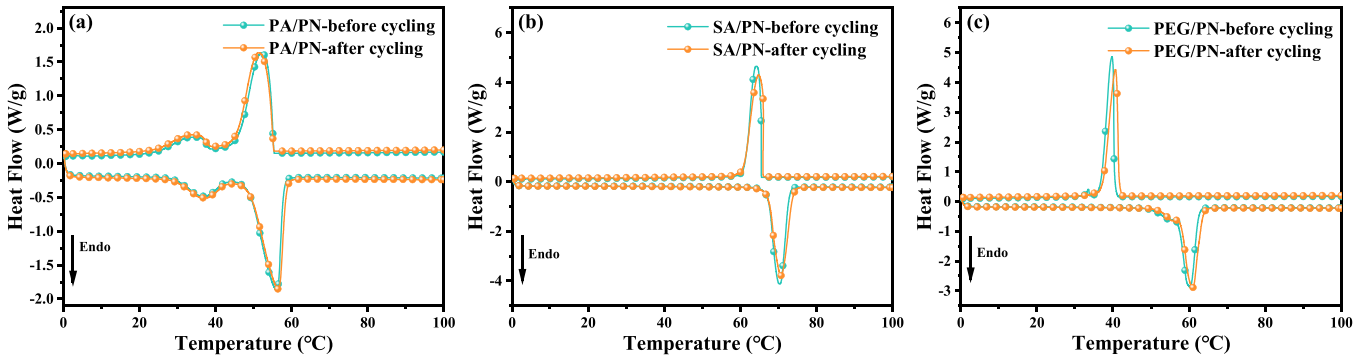

Fig. 12. DSC curves of (a) PA/PN, (b) SA/PN, and (c) PEG/PN composite PCMs prior to and following the 100 thermal cycling test.

CRediT authorship contribution statement

Laiquan Lv: Formal analysis, Investigation, Data curation, Writing-Original draft, Project administration. **Shengyao Huang:** Data curation, Writing-Original draft. **Chengyue Zhou:** Investigation, Writing-Original draft. Weiwei Ma: Conceptualization, Methodology, Validation.

Declaration of Competing Interest

The authors declare that they have no known competing financial interests or personal relationships that could have appeared to influence the work reported in this paper.

Data Availability

Data will be made available on request.

Acknowledgment

This study was supported by the Fundamental Research Funds for the Central Universities (2022ZFJH04).

Appendix A. Supporting information

Supplementary data associated with this article can be found in the online version at doi:10.1016/j.indcrop.2023.117184.

References

Ahmed, S.F., Rafa, N., Mehnaz, T., Ahmed, B., Islam, N., Mofijur, M., Hoang, A.T., Shafiullah, G.M., 2022. Integration of phase change materials in improving the performance of heating, cooling, and clean energy storage systems: an overview. J. Clean. Prod. 364, 132639.

Akhtar, A., Krepl, V., Ivanova, T., 2018. A combined overview of combustion, pyrolysis, and gasification of biomass. Energy Fuels 32, 7294–7318.

Amalina, F., Razak, A.S.A., Krishnan, S., Sulaiman, H., Zularisam, A.W., Nasrullah, M., 2022a. Biochar production techniques utilizing biomass waste-derived materials and environmental applications – a review. J. Hazard. Mater. Adv. 7, 100134.

Amalina, F., Syukor Abd Razak, A., Krishnan, S., Sulaiman, H., Zularisam, A.W., Nasrullah, M., 2022b. Advanced techniques in the production of biochar from lignocellulosic biomass and environmental applications. Clean. Mater. 6, 100137.

Arie, A.A., Kristianto, H., Cengiz, E.C., Demir-Cakan, R., 2020. Preparation of salacca peel-based porous carbons by K2CO3 activation method as cathode materials for LiS battery. Carbon Lett. 30, 207–213.

Atinafu, D.G., Dong, W.J., Wang, C., Wang, G., 2018. Synthesis of porous carbon from cotton using an Mg(OH)(2) template for form-stabilized phase change materials with high encapsulation capacity, transition enthalpy and reliability. J. Mater. Chem. A 6, 8969–8977.

Atinafu, D.G., Chang, S.J., Kim, S., 2020a. Infiltration properties of n-alkanes in mesoporous biochar: The capacity of smokeless support for stability and energy storage. J. Hazard Mater. 399, 123041.

Atinafu, D.G., Jin Chang, S., Kim, K.-H., Kim, S., 2020b. Tuning surface functionality of standard biochars and the resulting uplift capacity of loading/energy storage for organic phase change materials. Chem. Eng. J. 394.

Atinafu, D.G., Wi, S., Yun, B.Y., Kim, S., 2021a. Engineering biochar with multiwalled carbon nanotube for efficient phase change material encapsulation and thermal energy storage. Energy 216.

Atinafu, D.G., Yeol Yun, B., Uk Kim, Y., Wi, S., Kim, S., 2021b. Introduction of eicosane into biochar derived from softwood and wheat straw: influence of porous structure and surface chemistry. Chem. Eng. J. 415.

Ausavasukhi, A., Kampoosaen, C., Kengnok, O., 2016. Adsorption characteristics of Congo red on carbonized leonardite. J. Clean. Prod. 134, 506–514.

B, C., D, Z., L, Z., 2008. Transitional adsorption and partition of nonpolar and polar aromatic contaminants by biochars of pine needles with different pyrolytic temperatures. Environ. Sci. Technol. 42, 5137–5143.

Cao, L., Yu, I.K.M., Tsang, D.C.W., Zhang, S., Ok, Y.S., Kwon, E.E., Song, H., Poon, C.S., 2018. Phosphoric acid-activated wood biochar for catalytic conversion of starch-rich food waste into glucose and 5-hydroxymethylfurfural. Bioresour. Technol. 267, 242–248.

Chakraborty, P., Banerjee, S., Kumar, S., Sadhukhan, S., Halder, G., 2018. Elucidation of ibuprofen uptake capability of raw and steam activated biochar of Aegle marmelos shell: isotherm, kinetics, thermodynamics and cost estimation. Process Saf. Environ. Prot. 118, 10–23.

Chen, Y., Cui, Z., Ding, H., Wan, Y., Tang, Z., Gao, J., 2018. Cost-effective biochar produced from agricultural residues and its application for preparation of high performance form-stable phase change material via simple method. Int. J. Mol. Sci. 19.

Chen, Y., Xu, C., Cong, R., Ran, F., Fang, G., 2021. Thermal properties of stearic acid/active aluminum oxide/graphene nanoplates composite phase change materials for heat storage. Mater. Chem. Phys. 269.

Choi, J.Y., Nam, J., Yun, B.Y., Kim, Y.U., Kim, S., 2022. Utilization of corn cob, an essential agricultural residue difficult to disposal: composite board manufactured improved thermal performance using microencapsulated PCM. Ind. Crops Prod. 183.

Cong, R., Xu, C., Chen, Y., Ran, F., Fang, G., 2021. Enhanced thermal conductivity of palmitic acid/copper foam composites with carbon nanotube as thermal energy storage materials. J. Storage Mater. 40.

Das, D., Bordoloi, U., Muigai, H.H., Kalita, P., 2020. A novel form stable PCM based bio composite material for solar thermal energy storage applications. J. Storage Mater. 30.

Demir, M., Doguscu, M., 2022. Preparation of porous carbons using NaOH, K2CO3, Na2CO3 and Na2S2O3 activating agents and their supercapacitor application: a comparative study. Chemistryselect 7, e202104295.

Elliott, D.C., 2008. Catalytic hydrothermal gasification of biomass. Biofuels, Bioprod. Bioref. 2, 254–265.

Fan, L.-W., Zhu, Z.-Q., Zeng, Y., Lu, Q., Yu, Z.-T., 2014. Heat transfer during melting of graphene-based composite phase change materials heated from below. Int. J. Heat. Mass Transf. 79, 94–104.

Gao, J.K., Xu, Q.Y., Zhang, J.W., Wu, S.B., Chen, Y., Shi, Q., 2021. Fabrication of a novel highly thermal conductive shape-stabilized phase-change material using cheap and easily available cabbage mustard biochar as the matrix. JOM 73, 2487–2494.

Gayathiri, M., Pulingam, T., Lee, K.T., Sudesh, K., 2022. Activated carbon from biomass waste precursors: factors affecting production and adsorption mechanism. Chemosphere 294, 133764.

Grasso, M., Heede, R., 2023. Time to pay the piper: fossil fuel companies' reparations for climate damages. One Earth 6, 459–463.

Grycova, B., Pryszcz, A., Krzack, S., Klinger, M., Lestinsky, P., 2020. Torrefaction of biomass pellets using the thermogravimetric analyser. Biomass-.-. Convers. Biorefin. 11, 2837–2842.

Gu, X.B., Liu, P., Liu, C.J., Peng, L.H., He, H.C., 2019. A novel form-stable phase change material of palmitic acid-carbonized pepper straw for thermal energy storage. Mater. Lett. 248, 12–15.

Hai-Chen, Z., Ben-Hao, K., Xinxin, S., Xiang, L., 2019. Novel bio-based pomelo peel flour/polyethylene glycol composite phase change material for thermal energy storage. Polymers 11, 2043-2043.

Han, L., Zhang, X.L., Ji, J., Ma, K.L., 2022. Research progress on the influence of nano-additives on phase change materials. J. Storage Mater. 55, 105807.

He, C., Tang, C.Y., Li, C.H., Yuan, J.H., Tran, K.Q., Bach, Q.V., Qiu, R.L., Yang, Y.H., 2018. Wet torrefaction of biomass for high quality solid fuel production: a review. Renew. Sustain. Energy Rev. 91, 259–271.

Kılıç, M., Apaydın-Varol, E., Pütün, A.E., 2012. Preparation and surface characterization of activated carbons from Euphorbia rigida by chemical activation with ZnCl2, K2CO3, NaOH and H3PO4. Appl. Surf. Sci. 261, 247–254.

Kim, Y.U., Yun, B.Y., Nam, J., Choi, J.Y., Wi, S., Kim, S., 2021. Evaluation of thermal properties of phase change material-integrated artificial stone according to biochar loading content. Constr. Build. Mater. 305.
Kwak, J.H., Islam, M.S., Wang, S., Messele, S.A., Naeth, M.A., El-Din, M.G., Chang, S.X., 2019. Biochar properties and lead(II) adsorption capacity depend on feedstock type, pyrolysis temperature, and steam activation. Chemosphere 231, 393–404.
Lawag, R.A., Ali, H.M., Zahir, M.H., Qureshi, B.A., 2023. Investigation of PT 58 and PEG-6000-based finned heat sinks for thermal management of electronics. J. Clean. Prod. 390.
Li, B., Liu, T., Hu, L., Wang, Y., Gao, L., 2013. Fabrication and properties of microencapsulated Paraffin@SiO2 phase change composite for thermal energy storage. ACS Sustain. Chem. Eng. 1, 374–380.
Li, Y., Gupta, R., Zhang, Q., You, S., 2023. Review of biochar production via crop residue pyrolysis: development and perspectives. Bioresour. Technol. 369, 128423.
Lim, W.C., Srinivasakannan, C., Balasubramanian, N., 2010. Activation of palm shells by phosphoric acid impregnation for high yielding activated carbon. J. Anal. Appl. Pyrolysis 88, 181–186.
Liu, H., Qian, Z., Wang, Q., Wu, D., Wang, X., 2021a. Development of renewable biomass-derived carbonaceous aerogel/mannitol phase-change composites for high thermal-energy-release efficiency and shape stabilization. ACS Appl. Energy Mater. 4, 1714–1730.
Liu, H., Zheng, Z., Qian, Z., Wang, Q., Wu, D., Wang, X., 2021b. Lamellar-structured phase change composites based on biomass-derived carbonaceous sheets and sodium acetate trihydrate for high-efficient solar photothermal energy harvest. Sol. Energy Mater. Sol. Cells 229.
Londoño-Pulgarin, D., Cardona-Montoya, G., Restrepo, J.C., Muñoz-Leiva, F., 2021. Fossil or bioenergy? Global fuel market trends. Renew. Sustain. Energy Rev. 143, 110905.
López-Sabirón, A.M., Royo, P., Ferreira, V.J., Aranda-Usón, A., Ferreira, G., 2014. Carbon footprint of a thermal energy storage system using phase change materials for industrial energy recovery to reduce the fossil fuel consumption. Appl. Energy 135, 616–624.
Luo, Z., Yao, B., Yang, X., Wang, L., Xu, Z., Yan, X., Tian, L., Zhou, H., Zhou, Y., 2022. Novel insights into the adsorption of organic contaminants by biochar: a review. Chemosphere 287, 132113.
Lv, L., Wang, J., Ji, M., Zhang, Y., Huang, S., Cen, K., Zhou, H., 2022. Effect of structural characteristics and surface functional groups of biochar on thermal properties of different organic phase change materials: Dominant encapsulation mechanisms. Renew. Energy 195, 1238–1252.
Ma, B., Huang, Y., Nie, Z., Qiu, X., Su, D., Wang, G., Yuan, J., Xie, X., Wu, Z., 2019. Facile synthesis of Camellia oleifera shell-derived hard carbon as an anode material for lithium-ion batteries. RSC Adv. 9, 20424–20431.
Marsh, H., Rodríguez-Reinoso, F., 2006. Chapter 2 - activated carbon (origins). In: Marsh, H., Rodríguez-Reinoso, F. (Eds.), Activated Carbon. Elsevier Science Ltd, Oxford, pp. 13–86.
Mbarki, F., Selmi, T., Kesraoui, A., Seffen, M., 2022. Low-cost activated carbon preparation from Corn stigmata fibers chemically activated using H3PO4, ZnCl2 and KOH: Study of methylene blue adsorption, stochastic isotherm and fractal kinetic. Ind. Crops Prod. 178.
Mu, J.H., Li, Q., Kong, X.J., Wu, X.Z., Sunarso, J., Zhao, Y., Zhou, J., Zhuo, S.P., 2019. Characterization of hierarchical porous carbons made from bean curd via K2CO3 activation as a supercapacitor electrode. Chemelectrochem 6, 4022–4030.
Nazir, H., Batool, M., Osorio, F.J.B., Isaza-Ruiz, M., Xu, X.H., Vignarooban, K., Phelan, P., Inamuddin, Kannan, A.M., 2019. Recent developments in phase change materials for energy storage applications: a review. Int. J. Heat. Mass Transf. 129, 491–523.
Nicholas, A.F., Hussein, M.Z., Zainal, Z., Khadiran, T., 2019. Activated carbon for shape-stabilized phase change material. Synth., Technol. Appl. Carbon Nanomater. 279–308.
Sawadogo, M., Benmahiddine, F., Hamami, A.E.A., Belarbi, R., Godin, A., Duquesne, M., 2022. Investigation of a novel bio-based phase change material hemp concrete for passive energy storage in buildings. Appl. Therm. Eng. 212.
Seifi, H., Masoum, S., Tafreshi, S.A.H., Seifi, S., Jafari, S.M., 2020. Highly porous carbon from microalga, Chlorella vulgaris, as an electrochemical hydrogen storage material. J. Electrochem. Soc. 167, 120525.
Shen, Y.F., 2020. A review on hydrothermal carbonization of biomass and plastic wastes to energy products. Biomass-.-. Bioenergy 134, 105479.
Sinan, N., Unur, E., 2017. Hydrothermal conversion of lignocellulosic biomass into high-value energy storage materials. J. Energy Chem. 26, 783–789.
Singh, G., Ruban, A.M., Geng, X., Vinu, A., 2023. Recognizing the potential of K-salts, apart from KOH, for generating porous carbons using chemical activation. Chem. Eng. J. 451, 139045.
Singh, P., Sharma, R.K., Khalid, M., Goyal, R., Sari, A., Tyagi, V.V., 2022. Evaluation of carbon based-supporting materials for developing form-stable organic phase change materials for thermal energy storage: a review. Sol. Energy Mater. Sol. Cells 246, 111896.
Song, J., Cai, Y., Du, M., Hou, X., Huang, F., Wei, Q., 2020. 3D lamellar structure of biomass-based porous carbon derived from towel gourd toward phase change composites with thermal management and protection. ACS Appl. Bio Mater. 3, 8923–8932.
Stonehouse, A., Abeykoon, C., 2022. Thermal properties of phase change materials reinforced with multi-dimensional carbon nanomaterials. Int. J. Heat. Mass Transf. 183, 122166.
Su, W., Hu, M., Wang, L., Kokogiannakis, G., Chen, J., Gao, L., Li, A., Xu, C., 2022. Microencapsulated phase change materials with graphene-based materials: Fabrication, characterisation and prospects. Renew. Sustain. Energy Rev. 168.
Tan, B., Huang, Z., Yin, Z., Min, X., Liu, Yg, Wu, X., Fang, M., 2016. Preparation and thermal properties of shape-stabilized composite phase change materials based on polyethylene glycol and porous carbon prepared from potato. RSC Adv. 6, 15821–15830.
Venkatachalam, C.D., Sekar, S., Sengottian, M., Ravichandran, S.R., Bhuvaneshwaran, P., 2023. A critical review of the production, activation, and morphological characteristic study on functionalized biochar. J. Storage Mater. 67, 107525.
Wan, Y.C., Chen, Y., Cui, Z.X., Ding, H., Gao, S.F., Han, Z., Gao, J.K., 2019. A promising form-stable phase change material prepared using cost effective pinecone biochar as the matrix of palmitic acid for thermal energy storage. Sci. Rep. 9, 11535.
Wang, H., Gao, Q., Hu, J., 2009. High Hydrogen Storage Capacity of Porous Carbons Prepared by Using Activated Carbon. J. Am. Chem. Soc. 131, 7016–7022.
Wang, R.Z., Huang, D.L., Liu, Y.G., Zhang, C., Lai, C., Wang, X., Zeng, G.M., Zhang, Q., Gong, X.M., Xu, P., 2020. Synergistic removal of copper and tetracycline from aqueous solution by steam-activated bamboo-derived biochar. J. Hazard Mater. 384, 121470.
Wang, X., Kuang, D., Chen, H., Xue, H., 2023. Capsulated phase-change materials containing paraffin core/polymethyl methacrylate shell: thermoregulation modifier for asphalt binder. Constr. Build. Mater. 369.
Wei, G., Wang, G., Xu, C., Ju, X., Xing, L., Du, X., Yang, Y., 2018a. Selection principles and thermophysical properties of high temperature phase change materials for thermal energy storage: a review. Renew. Sustain. Energy Rev. 81, 1771–1786.
Wei, Y., Li, J., Sun, F., Wu, J., Zhao, L., 2018b. Leakage-proof phase change composites supported by biomass carbon aerogels from succulents. Green. Chem. 20, 1858–1865.
Xi, Y.B., Wang, Y.Y., Yang, D.J., Zhang, Z.K., Liu, W.F., Li, Q., Qiu, X.Q., 2019. K2CO3 activation enhancing the graphitization of porous lignin carbon derived from enzymatic hydrolysis lignin for high performance lithium-ion storage. J. Alloys Compd. 785, 706–714.
Xu, J., Sun, J., Zhao, J., Zhang, W., Zhou, J., Xu, L., Guo, H., Liu, Y., Zhang, D., 2023. Eco-friendly wood plastic composites with biomass-activated carbon-based form-stable phase change material for building energy conversion. Ind. Crops Prod. 197.
Yadav, A., Verma, A., Kumar, A., Dashmana, H., Kumar, A., Bhatnagar, P.K., Jain, V.K., 2021. Recent advances on enhanced thermal conduction in phase change materials using carbon nanomaterials. J. Storage Mater. 43, 103173.
Yang, H.Y., Wang, Y.Z., Yu, Q.Q., Cao, G.L., Sun, X.H., Yang, R., Zhang, Q., Liu, F., Di, X., Li, J., Wang, C.Y., Li, G.L., 2018. Low-cost, three-dimension, high thermal conductivity, carbonized wood-based composite phase change materials for thermal energy storage. Energy 159, 929–936.
Yang, S., Wi, S., Lee, J., Lee, H., Kim, S., 2019. Biochar-red clay composites for energy efficiency as eco-friendly building materials: thermal and mechanical performance. J. Hazard Mater. 373, 844–855.
Yang, Y., Yin, Q., Xu, F., Sun, L., Xia, Y., Guan, Y., Liao, L., Zhou, T., Lao, J., Wang, Y., Wang, Y., Song, L., Li, D., 2022. Fabricated polyethylene glycol/ hydroxylated carbon nanotubes shape-stabilized phase change materials with improving thermal conductivity. Thermochim. Acta 718.
Yek, P.N.Y., Li, C., Peng, W., Wong, C.S., Liew, R.K., Wan Mahari, W.A., Sonne, C., Lam, S.S., 2021. Production of modified biochar to treat landfill leachate using integrated microwave pyrolytic CO_2 activation. Chem. Eng. J. 425.
Yu, K., Liu, Y., Jia, M., Yang, Y., 2021. Bio-based dual-functionalized phase change composite: ultrafast solar-to-thermal conversion and reinforced heat storage capacity. Energy Fuels 35, 16162–16173.
Yun, B.Y., Kang, Y., Kim, Y.U., Wi, S., Kim, S., 2022. Practical solutions with PCM for providing thermal stability of temporary house, school and hospital in disaster situations. Build. Environ. 207, 108540.
Zhang, X., Huang, Z., Yin, Z., Zhang, W., Huang, Y., Liu, Y., Fang, M., Wu, X., Min, X., 2017. Form stable composite phase change materials from palmitic-lauric acid eutectic mixture and carbonized abandoned rice: preparation, characterization, and thermal conductivity enhancement. Energy Build. 154, 46–54.
Zhao, X., Ouyang, W., Hao, F., Lin, C., Wang, F., Han, S., Geng, X., 2013. Properties comparison of biochars from corn straw with different pretreatment and sorption behaviour of atrazine. Bioresour. Technol. 147, 338–344.
Zhou, H., Lv, L., Zhang, Y., Ji, M., Cen, K., 2021. Preparation and characterization of a shape-stable xylitol/expanded graphite composite phase change material for thermal energy storage. Sol. Energy Mater. Sol. Cells 230.